This paper appears in the International Journal of Computer Assisted Radiology and Surgery, 2015.
DOI: 10.1007/s11548-015-1329-4

Estimating Needle Tip Deflection in Biological Tissue from a Single Transverse Ultrasound Image: Application to Brachytherapy

Carlos Rossa[1], Ronald Sloboda[2], Nawaid Usmani[2], and Mahdi Tavakoli[1]

***Abstract*—This paper proposes a method to predict the deflection of a flexible needle inserted into soft tissue based on the observation of deflection at a single point along the needle shaft. We model the needle-tissue as a discretized structure composed of several virtual, weightless, rigid links connected by virtual helical springs whose stiffness coefficient are found using a pattern search algorithm that only requires the force applied at the needle tip during insertion and the needle deflection measured at an arbitrary insertion depth. Needle tip deflections can then be predicted for different insertion depths. Verification of the proposed method in synthetic and biological tissue show a deflection estimation error of less than 2 mm for images acquired at 35% or more of the maximum insertion depth, and decreases to 1 mm for images acquired closer to the final insertion depth. We also demonstrate the utility of the model for prostate brachytherapy, where in-vivo needle deflection measurements obtained during early stages of insertion are used to predict the needle deflection further along the insertion process. The method can predict needle deflection based on the observation of deflection at a single point. The ultrasound probe can be maintained at the same position during insertion of the needle, which avoids complications of tissue deformation caused by the motion of the ultrasound probe.**

I. INTRODUCTION

Needle insertion is a minimally invasive procedure used for purposes such as biopsy, brachytherapy, neurosurgery and radio-frequency ablation. The outcomes of needle-based procedures generally depend on the accuracy with which the needles reach intended target locations [2]. Inaccurate needle placement may limit the effectiveness of the procedure or lead to undesirable side effects [4]. In needle-based procedures, a critical assumption typically made is that the needle will remain unbent across the entire length of its insertion in tissue. However, in practice this assumption does not hold true as needle deflection occurs due to needle-tissue interaction.

Needle insertion is often performed under ultrasound image guidance [22] [24] [18]. The primary limitation in using ultrasound (US) images for assessment of needle position is the low quality of images that often contain artifacts that are hard to interpret and distinguish from targets [5] [6]. In addition, the field of view of the US transducer is often very narrow and thereby only a small portion of the needle can be imaged at once. For instance, in prostate brachytherapy, long needles are inserted to about 140 to 160 mm depth through the patient's perineum in order to deliver radioactive seeds within the prostate [21]. Given the limited field of the view of the US image, typically only 25% of the inserted needle length can be longitudinally imaged at once.

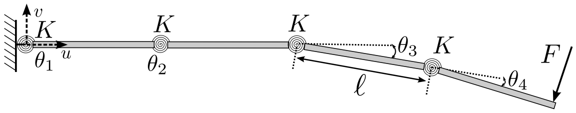

Fig. 1. Schematic representation of the lumped model of a needle in free space. In this example, the needle is discretized into 4 weightless bars of length l connected by helical springs of stiffness K. Angle $\theta(i)$ denotes how much the bar i rotates which respect to the bar $i-1$. A force F is applied vertically at the tip.

Longitudinal US imaging shows a plane parallel to the needle's shaft, and is typically used for rapid visualization of needles in tissue. However, depending on how the needle deflects during insertion, aligning the US probe with this longitudinal plane that contains the needle is not always possible given the limited dexterity of transrectal probes. Alternatively, transverse images obtained in planes perpendicular to the needle shaft eliminate complications of probe alignment at the cost of only seeing a single cross section of the needle shaft along each transverse slice (image) [28]. Despite this limitation, transverse images are widely used for pre-implant treatment planning in brachytherapy, since they provide a consistent view of cross sections of the prostate.

Tracking the needle tip during insertion in transverse images requires the US probe to move in synchrony with the needle, such that the needle tip is always visible in the images. Recent techniques make use of motorized US probes that move with the needle tip [27], or translate along the shaft of an inserted needle [29].

Although moving the probe with the needle can provide an accurate assessment of needle position, probe motion during the clinical procedure can result in unwanted deformation of the surrounding tissues [13]. This is a critical concern in prostate brachytherapy where deformation of the prostate during the intra-operative procedure results in anatomic variations of the preoperative-planned needle target location [16] [25]. As a result, limiting the motion of the ultrasound probe is desirable in order to minimize discrepancies between pre-and intra-perative position of the prostate.

In this paper we propose a method for needle deflection estimation based on the observation of the needle in a single transverse US image obtained during insertion. Using this method, the path that the needle tip follows can be reconstructed without issues of probe alignment and tissue

---

This work was supported by the Natural Sciences and Engineering Research Council (NSERC) of Canada under grant CHRP 446520, the Canadian Institutes of Health Research (CIHR) under grant CPG 127768, and by the Alberta Innovates - Health Solutions (AIHS) under grant CRIO 201201232.

[1] Carlos Rossa, and Mahdi Tavakoli (Corresponding Author) are with the Department of Electrical and Computer Engineering, University of Alberta, AB, Canada T6G 2V4. E-mail: rossa@ualberta.ca; madhi.tavakoli@ualberta.ca.

[2] Ron Sloboda and Nawaid Usmani are with the Cross Cancer Institute and the Department of Oncology, University of Alberta, Edmonton, AB, Canada T6G 1Z2. E-mail: {ron.sloboda, nawaid.usmani}@albertahealthservices.ca.

deformation present in sagittal imaging. The US probe can either be maintained at the same position throughout the needle insertion process, or be moved along with the needle during the initial stages of insertion and stopped at an appropriate position. A single image is fed into a lumped needle-tissue interaction model that estimates the needle tip deflection further along the insertion process. We extend an available discrete needle model model [7] where the needle is modelled by a discrete structure composed of several rigid bars connected in series by helical springs to capture needle-tissue interaction. The reaction of tissue is modelled as a modification of the stiffness of virtual joints that are inside the tissue which are identified using an adaptive optimization algorithm.

The paper is organized as follows. We first introduce a lumped model for a needle in free space, which is then further extended to capture needle-tissue interaction. Section IV introduces the adaptive algorithm that identifies the model parameters. Reported experimental results in Section VI in two synthetic phantom and two biological tissue samples, show that needle deflection can be predicted within an average error of less than 0.8 mm as long the image used as input to the model is acquired at a depth of 35% or higher of the maximum needle insertion depth. Finally, an application to prostate brachytherapy is proposed. In-vivo needle data from prostate brachytherapy procedures are used to predict needle deflection for different insertion attempts and insertion depths into the prostate of actual human patients.

II. LUMPED NEEDLE MODEL IN FREE SPACE

The proposed method for needle tip path estimation makes use of a single measurement of needle deflection, which is used in a needle-tissue model along with the force applied at the needle tip during insertion. In this section, we introduce a lumped model for the needle in free space.

The proposed lumped model considers the needle as a discrete structure composed of several rigid bars connected in series by helical springs, referred to as virtual joints. As a result, the partial differential equations of the infinite dimensional time-space model of the needle-tissue system [14] are reduced to ordinary differential equations with only a few parameters. A similar model was introduced in [7] and [10]. These papers only concerned a needle in free space and not in contact with tissue. Here the model will be extended to capture needle-tissue interaction. Also, we propose an online identification method of the needle-tissue model parameters using a pattern search algorithm based on a single US image acquired during insertion.

A schematic representation of the lumped needle model when the needle is in free space is shown in Fig. 1. The needle of length L is discretized into n undeformable weightless bars, each of which has the length ℓ so that $\ell = Ln^{-1}$. In Fig. 1, $n = 4$. Let us denote by θ_i the angle by which the bar i rotates relative to the bar $i-1$ along an axis perpendicular to the plane. A force F_r is applied to the needle tip (endpoint of the last bar) along an axis normal to the unbent needle (corresponding to all $\theta_i = 0$). At each joint, two neighbouring bars are connected through a helical spring. All helical springs have the same stiffness of K.

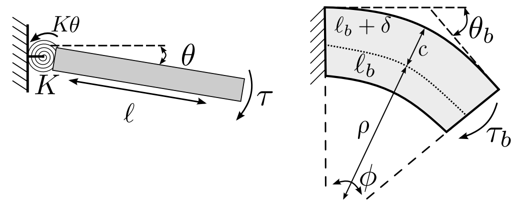

(a) Single virtual link (b) Beam model

Fig. 2. A virtual link and the equivalent cantilever beam model. In (a), a torque τ is applied to the virtual link of length ℓ connected to a fixed wall through a spring of stiffness K. The resultant deflection angle is is τ/K. In (b), the torque τ_b bends the beam to an angle of θ_b.

A. Forward Kinematics

In the four-link example shown in Fig. 1, the torque τ_i generated at each joint i by a force $F = [F_u \ F_v]^T$, where F_u and F_v are the horizontal and vertical components of F, respectively, is [26]

$$
\begin{aligned}
\tau_4 =& F_v\ell[\cos(\underbrace{\theta_1+\theta_2+\theta_3+\theta_4}_{\Theta_4})] - F_u\ell[\sin\Theta_4)],\\
\tau_3 =& F_v\ell[\cos\Theta_4+\cos(\underbrace{\theta_1+\theta_2+\theta_3}_{\Theta_3})] - F_u\ell[\sin\Theta_4+\cos\Theta_3],\\
\tau_2 =& F_v\ell[\cos\Theta_4+\cos\Theta_3+\cos(\underbrace{\theta_1+\theta_2}_{\Theta_2})]\\
&- F_u\ell[\sin\Theta_4+\sin\Theta_3+\sin\Theta_2],\\
\tau_1 =& F_v\ell[\cos\Theta_4+\cos\Theta_3+\cos\Theta_2+\cos(\theta_1)]\\
&- F_u\ell[\sin\Theta_4+\sin\Theta_3+\sin\Theta_2+\sin(\theta_1)].
\end{aligned}
\tag{1}
$$

For a needle model composed of n links, the torque at the joint i is

$$
\tau_i = G_i \begin{bmatrix} F_u \\ F_v \end{bmatrix} \tag{2}
$$

where $1 \le i \le n$ and G_i is the Jacobian matrix given by:

$$
G_i = \begin{bmatrix} -\ell\sum_{j=i}^{n}\sin\left(\sum_{p=1}^{j}\theta_p\right) & 0 \\ 0 & \ell\sum_{j=i}^{n}\cos\left(\sum_{p=1}^{j}\theta_p\right) \end{bmatrix}. \tag{3}
$$

The torques found through (2) are divided by the joint stiffness K to find the angular displacements of the joints, i.e., $\theta_i = \tau_i/K$. The Cartesian position of joint i (the endpoint of link $i-1$) in the normal and axial directions with respect to the straight needle, called v_i and u_i respectively, can be obtained as

$$
v_i = v_{i-1} + \ell\sin\left(\sum_{p=1}^{i}\theta_p\right), \quad u_i = u_{i-1} + \ell\cos\left(\sum_{p=1}^{i}\theta_p\right). \tag{4}
$$

The reason for the summation is that θ_i is defined to be the rotation angle of link i *relative to* link $i-1$. Equations (3)-(4) simply state that the Cartesian position of joint i is that of joint $i-1$ plus the displacement caused by link i. The normal displacement (deflection) of the needle tip will be v_n.

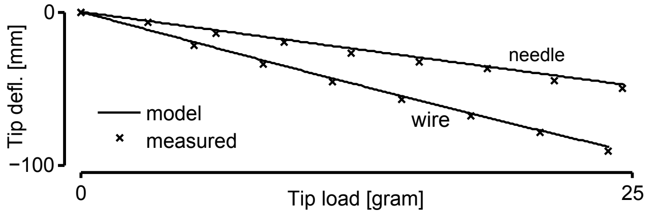

Fig. 3. Needle tip deflection in free space as a function of the load applied at the tip. The needle is discretized into 50 virtual joints. Different masses are hung at the tip and the tip deflection is recorded experimentally and calculated theoretically.

B. Determining the Joint Stiffness

In order to determine the stiffness K of the joints that are used in the lumped needle model, consider the single virtual link shown in Fig. 2(a). A torque τ is applied at the end point of this rigid link of length ℓ, which is connected to a fixed wall through a helical spring of stiffness K. The reaction torque $K\theta$ at the clamping point, where θ is the deflection angle, is equal and opposed to τ [3]. This means

$$\frac{\theta}{\tau} = \frac{1}{K}. \tag{5}$$

Now, consider the equivalent beam model in Fig. 2(b). At its neutral axis shown by the dotted line and located at a radius of ρ, the short beam has the length $\ell_b = \ell$, which is the same as that of the virtual link in Fig. 2(a). Let us denote by c the radial distance between the neutral axis and the outer radius and by $\ell + \delta$ the outer arc length. If the beam is under a constant bending moment τ_b, then the resultant bending angle is θ_b, which is equal to its angle of curvature ϕ [10]. The strain $\varepsilon(y)$, defined as the amount of elongation divided by the initial length, at a radial distance y to the neutral axis is $\varepsilon(y) = \tau_b y (EI)^{-1}$ where E is the beam Young's modulus and I is its second moment of inertia. At the outer arc, where the strain is $\varepsilon(c) = \delta\ell^{-1}$ by definition, it yields

$$\frac{\delta}{\ell} = \frac{\tau_b}{EI}c. \tag{6}$$

From similarity of the arcs, we have [7]:

$$\frac{\ell_b + \delta}{\ell_b} = \frac{\rho + c}{\rho} \Longrightarrow \frac{\delta}{\ell_b} = \frac{c}{\rho} \tag{7}$$

Replacing (7) in (6) and knowing that $\rho = \ell\theta^{-1}$, the relation between the bending moment and the resultant bending angle can be written as

$$\frac{\theta_b}{\tau_b} = \frac{\ell}{EI}. \tag{8}$$

Therefore, if the moments applied on the virtual link in Fig. 2(a) and on the beam model in Fig. 2(b) are the same ($\tau_b = \tau$), then the stiffness of the equivalent lumped model that gives the same bending angle ($\theta_b = \theta$) in the two models, for a beam of length $\ell = Ln^{-1}$, is obtained by combining (8) and (5) as

$$K = \frac{EI}{L}n \tag{9}$$

The stiffness found in (9) corresponds to the stiffness of all the $n-1$ springs that compose the needle lumped model.

C. Experimental Verification

Two different needles are used to validate the proposed lumped model for the needle in free space. The first needle is a standard 18-gauge brachytherapy needle (Eckert & Ziegler GmbH, Berlin, Germany). The needle has a length of $L = 210$ mm and a Young's modulus of $E = 200$ GPa. The inner and outer needle radii are $r_1 = 0.5$ mm and $r_2 = 0.635$ mm, respectively. Its second moment of inertia can then be calculated as $I = \pi(r_2^4 - r_1^4)/4 = 7.86 \times 10^{-14}$ m^4. The second needle used in the experiment is a 226 mm long, solid stainless steel wire with a Young's modulus of 200 GPa. The wire has an outer radius of 0.5 mm which gives a second moment of inertia of 4.91×10^{-14}. Both needles are modelled with $n = 50$ virtual joints. Thus, the stiffness K given by (9) for the needle and for the wire are 3.93 and 2.45 Nm rad^{-1}, respectively.

Different masses m are hung at tip of each needle and the tip normal deflections v_n are recorded. The vertical force applied at the needle tip then yields $F_u = 0$ and $F_v = -mg$, where g is the gravity constant. The needle tip deflection is calculated interactively from (1)-(3). The observed predicted needle tip deflection values for different masses hung at the needle tip are presented in Fig. 3. The results show that the proposed model can satisfactorily predict the deflection of the needles subjected to external loads. The obtained needle tip deflection in free space is not sensitive to the number of virtual joints. However, in order to reconstruct the needle shaft, it is recommended to discretize the needle with at least 50 virtual joints. In the following section, this model is extended to a needle inserted into soft tissue.

III. LUMPED MODEL FOR NEEDLE-TISSUE INTERACTION

Needle-tissue interaction forces have been previously modelled as a combination of lateral springs distributed along the needle and friction forces [9]. Local deformation of the springs was calculated using FEM [12]. In our work, the reaction of tissue is modelled by increasing the stiffness of the virtual joints in the needle model that act against the deflection of the needle. We introduce an adaptive algorithm that updates the stiffness of the virtual joints that are inside the tissue as the needle is inserted. The model inputs are an estimate of the force applied at the needle tip and the deflection measured at one arbitrary point during insertion.

Needle insertion into tissue results in a force F applied perpendicularly to the needle beveled tip as shown in Fig. 4(a). The force F can be decomposed into a transverse force Q, perpendicular to the last bar of the last virtual joint of the needle, and a force P parallel to the last virtual joint of the needle, which depend on the tip bevel angle β. The transverse force Q causes the needle to bend. Assuming that the needle will not substantially deviate from a straight line, the effect of P on deflection will be neglected as it mostly causes longitudinal compression of the needle. These forces are typically assumed constant during the insertion and are insensitive to the overall bending of the needle [23]. The force applied at the needle tip in (2) is

$$F(Q) = \begin{bmatrix} F_u \\ F_v \end{bmatrix} = Q \begin{bmatrix} \sin(\sum_{p=1}^{n} \theta_p) \\ -\cos(\sum_{p=1}^{n} \theta_p) \end{bmatrix}. \tag{10}$$

Having modelled the needle, the tissue reaction needs to be modelled.

Consider a needle inserted into tissue as in Fig. 4(a). As the needle is advanced into the tissue, it bends and increasingly compresses the part of tissue shown under the needle. The compressed tissue acts as a support and applies reaction forces against the needle [17] [2] that, for an elastic tissue, are proportional to the tissue compression. Due to the increasing tissue compression forces as the needle advances into the tissue, it is reasonable to assume that the tissue applies the highest reaction forces at the needle entry point and the least reaction force at the needle tip. Therefore, Fig. 4(a) shows the tissue reaction force to be at its maximum at the needle entry point and at its minimum at the needle tip.

In the proposed model, the above-discussed tissue reaction forces act as helical springs of stiffness T_i added to the initial nominal joint stiffness K representing the needle alone and found in (9). Together, these two sources of virtual joint stiffness resist against the deflection of the needle. The joints that are inside the tissue have stiffness $K+T_i$. For a joint i outside the tissue, $T_i = 0$. For simplicity, in the rest of this paper, we assume the needle bending outside the tissue to be negligible by considering the stiffness of the joints outside the tissue to be very large.

In order to follow the proposed load distribution in Fig. 4(a), the stiffness T_i describing the contribution of the tissue reaction to the stiffness of the joint i is modelled as

$$T_i = k_0[\ell(n-i+1)]^{k_1} \tag{11}$$

where k_0 and k_1 depend on the mechanical properties of the needle and tissue. From (11), the angular displacements of the joints become

$$\theta_i = \frac{G_i}{K+T_i}F(Q) \tag{12}$$

Then, the deflection of the needle at a given insertion depth can be calculated using (4). The radius of curvature ρ of the needle shape at the joint i is

$$\rho_i = \left[1+\left(\frac{v_i - v_{i-1}}{u_i - u_{i-1}}\right)^2\right]^{\frac{3}{2}} \left|\frac{v_{i+1} - 2v_i + v_{i-1}}{(u_i - u_{i-1})^2}\right|^{-1} \tag{13}$$

In (11), k_0 depends on the stiffness of the tissue. It determines the amount of needle deflection for a given load applied at the tip: the higher k_0 is, the less the needle deflection is; k_1 can be tuned to obtain a specific radius of curvature. Since $\ell(n-i+1) < L \ \forall n$ and $L < 1$, the stiffness of the tissue is inversely proportional to k_1. Therefore, the radius of curvature is proportional to k_1. In other words, for low values of k_1, the shape of the needle is highly curved. This means that the needle tip can reach different deflections at the same depth by following different paths. The influence of k_0 and k_1 in (11) on the needle deflection is shown in Fig. 5. A load of $Q = 1$ N is applied at the needle tip of 18-gauge needle when it is inserted to a depth of 140 mm. The figure shows the average radius of curvature (bottom) and the final needle tip deflection v_n (top).

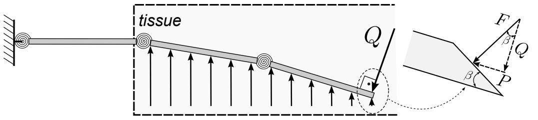

(a) Forces acting on the needle during insertion into tissue

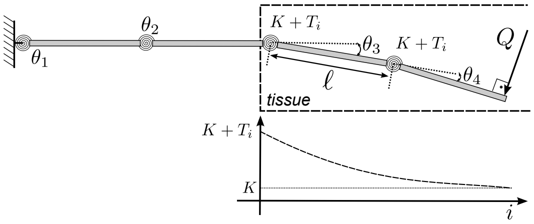

(b) Equivalent lumped model.

Fig. 4. Needle-tissue interaction lumped model. In (a) the forces acting on the needle tip during insertion. F is the cutting force, P and Q are the transverse and axial components of F. In (b) the reaction of the tissue is modelled as springs of stiffness T_i. Joints inside the tissue have stiffness $K+T_i$ and joints outside the tissue have stiffness K.

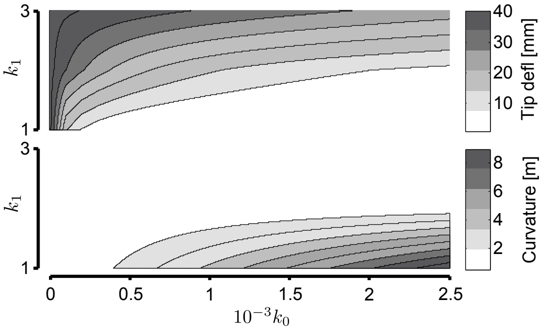

Fig. 5. Influence of tissue model parameters on the needle tip deflection and average radius of curvature. The simulation show the tip deflection (top) at an insertion depth of 140 mm and mean radius of curvature of the needle shape (bottom), for $Q = 1$ N.

IV. ADAPTIVE IDENTIFICATION OF MODEL PARAMETERS

To predict the needle deflection, the proposed model requires knowledge of the tip load Q and the mechanical properties of the needle and the stiffness T_i. For a given pair of tissue and needle, we will directly measure Q and empirically identify by model fitting the other unknown model parameter, i.e., k_0 and k_1 in (11) needed to find T_i.

The tip load Q is measured using an experimental procedure detailed in Section V-C. We will perform needle insertion in the same tissue to measure the deflection v_j of a single point j of the needle at a given insertion depth. Knowledge of Q and the single deflection measurement are combined in an interactive simulation where we will update k_0 and k_1 until the simulated deflection matches the measured deflection. The procedure to find the model parameters in Fig. 6(a) is composed of two loops, i.e., needle insertion simulation and numerical search loop. A simplified pseudocode used for parameter identification is presented in Algorithm 1.

Simulation insertion loop: This loop simulates the needle insertion for a given set of Q, k_0 and k_1. The insertion begins with the straight needle placed outside the tissue, thus $\theta_i = 0$ and $i_{in} = 0$, where i_{in} is the number of virtual joints that are inside the tissue (see ① in Fig. 6(a)). The needle is pushed

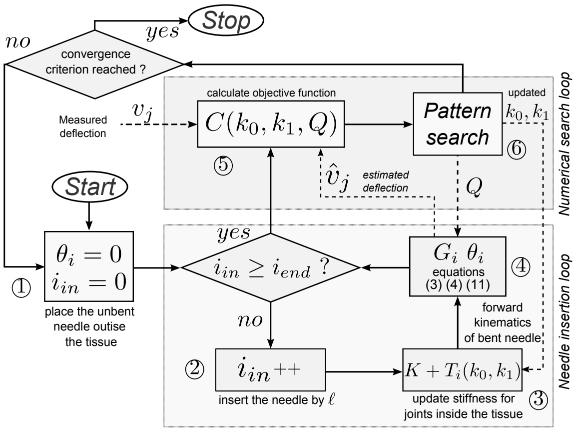

(a) Procedure to identify the model parameters

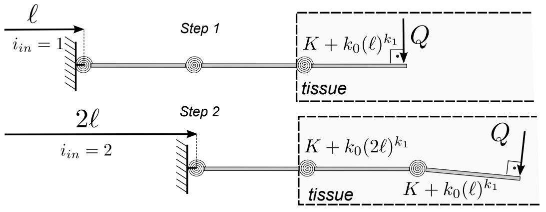

(b) Needle insertion loop sequence

Fig. 6. Procedure to identify the model parameters. In (a) i_{in} and i_{end} are the number of links inside the tissue and the number of links that needs to be inserted to reach a desired depth. The objective function is defined in (14). The needle insertion sequence is shown in (b).

by ℓ units of length into the tissue ($i_{in} = i_{in} + 1$). At each increment of i_{in}, the joint i that is inside the tissue acquires a stiffness of $K + T_i$ (see ③). The needle insertion sequence is detailed in Algorithm 1, and depicted in Fig. 6(b). The load Q is subsequently applied at the end of the last virtual joint and the Cartesian position of the virtual joints is calculated through the forward kinematics (see ④ in Fig. 6(a)). The process is repeated until $i_{in} \geq i_{end}$ where $i_{end} = d\ell^{-1}$ is the number of joints that need to be inserted to reach a desired insertion depth d. Once the needle reaches d, the insertion loop is finished and another interaction of the numerical search loop begins.

Numerical search loop: The numerical search loop interactively updates k_0 and k_1 to match the measured deflection v_j from the single US image with the simulated deflection $\hat{v}_n$. It does so by making use of a Pattern Search Algorithm (PSA) implemented using the *psoptimset* in Matlab function. PSA is a class of optimization method that carries out a coordinate search to minimize a non-linear objective function. It is characterized by a sequence of iterates h with non-increasing objective function values. Each iteration comprises two steps, i.e., global search and local pull steps. In the global search step, the objective function $C(x)$ is evaluated at a finite number of trial points x_h in an attempt to find new points x_{h+1}, called the incumbent, which will give a lower objective function value than the current trial points x_h. The current incumbent is only updated if a lower value of $C(x)$ is found. The pull step is executed if the global step fails to find a lower value for $C(x)$. In this case, the objective function is evaluated at a set of points close to x_h. The algorithm stops when a convergence criterion is reached, which means that no improved iterate (i.e., lower value for $C(x)$) can be found or the variation of the cost function between two iterations is less than a predefined value.

Algorithm 1 Identify Model Parameters

```
procedure NUMERICALSEARCHLOOP
    $Q, v_j \leftarrow$ From experiments
    $k_0, k_1 \leftarrow$ Initialize
    while Convergence criteria not reached do
        $\hat{v}_n \leftarrow$ InsertionLoop
        $C(k_0, k_1) = |\hat{v}_n - v_j| / |\hat{v}_n|$
        $k_0, k_1 \leftarrow$ psoptimset
    end while
end procedure
procedure INSERTIONLOOP
    $\theta_i = v_i = 0\ \forall i,\ i_{in} = 0$
    for $i_{end} < i_{in}$ do
        $i_{in} = i_{in} + 1$
        $\theta_i = F(Q) G_i / (K + T_i(k_0, k_1))$
        $v_i = v_{i-1} + \ell \sin(\sum_0^i \theta_p)$
    end for
    return($v_j$)
end procedure
```

In our case, the trial points in the PSA are the values of k_0 and k_1 ($x = [k_0, k_1]$). We define the objective function as the difference between the simulated tip deflection (at the joint n), called $\hat{v}_n(k_0)_j$, found when j joints are inserted into tissue, and the measured deflection v_j at the same depth obtained from experiments. The objective function $C(k_0, k_1)$ is defined as (see ⑤ in Fig. 6(a)):

$$C(k_0, k_1) = \left| \frac{|\hat{v}_n(k_0, k_1)_j| - |v_j|}{\hat{v}_n(k_0, k_1)_j} \right| \tag{14}$$

Based on the current value of the objective function, the PSA updates k_0 and k_1 (see Algorithm 1). Then, the needle insertion loop is performed again to allow the cost function to be re-evaluated with the new set of parameters. When the convergence criterion is reached, k_0 and k_1 represent the values that best fit the measured and the simulated deflection. For a given combination of needle and tissue, once k_0 and k_1 are identified, the needle shape (position of the entire needle's axis at a given depth) and further needle tip deflections (path followed by the needle tip) can be predicted for different insertion depths.

V. EXPERIMENTAL SETUP

The 2-DOF prismatic-revolute robotic system used for conducting the experiments is shown in Fig. 7. The needle is connected to a 6-DOF force/torque sensor (JR3, Inc. Woodland, USA) that measures the axial insertion force (the other 5-DOF are not used). This assembly is mounted on a carriage that slides on a linear stage. The carriage's translational motion is actuated by a Maxon motor RE-40 through a belt and pulley mechanism.

For assessment of the model performance in phantom tissues, a camera placed 300 mm behind the tissue container records at 30 Hz longitudinal images of the needle inside

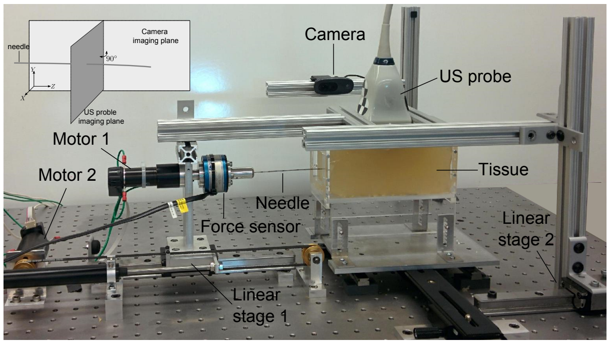

Fig. 7. Needle insertion robot. A motor provides the linear motion to insert the needle into the phantom tissue. The axial force (along Z) at the needle base is measured by a force sensor. Images of the needle inside tissue are recorded from the side by a camera in the (Y,Z) plane and by an ultrasound probe in the (X,Y) plane.

a semitransparent tissue (in the (Y,Z) plane defined in the upper left corner of Fig. 7). The needle is steered such that its deflection plane is parallel to the image plane. For validation of the model in biological tissue, a 4DL14-5/38 Linear 4D ultrasound transducer connected to a SonixTouch ultrasound machine (Ultrasonix, Richmond, Canada) is placed above the tissue to acquire 2D axial images of the needle in the (X,Y) plane in Fig. 7. The ultrasound probe is connected to a second linear stage whose horizontal position is measured by a linear potentiometer (Midori Precisions, Tokyo, Japan). In order to follow the needle tip as the needle is inserted, the imaging plane is initially placed at the needle tip, and both linear stages are connected so that the probe moves with the same velocity as the needle's base. Note that probe motion is only used for validation of the model. In fact, the probe can be held at a fixed insertion depth as the needle is inserted.

A. Image Processing

For experiments involving Tissues 1 and 2, camera images are used as ground truth. To segment the needle shape in each camera image, the images are first pre-conditioned by contrast enhancement and noise filtering via a Wiener lowpass filter [11]. A Sobel operator is then applied to the filtered images to detect the needle edges. All obtained pixels are candidate points for the needle contour; however, only some of them correspond to the actual needle. The Random Sample Consensus (RANSAC) algorithm [8] is then used to determine the image pixels that better correspond to the needle shape. This is done by fitting the candidate points to a second-order polynomial that fits the needle shape. By interactively evaluating the distance between the candidate points and the polynomial, pixels that do not represent the needle can be identified and discarded. An example of the original camera image overlaid on the polynomial curve is shown in Fig. 8(a). This procedure outputs the needle shape from which the position of the needle tip can be calculated. Light refraction effects in the tissue are neglected.

The needle appears in each 2D US image as a bright spot along with extraneous background objects. To remove the majority of these objects, we first define a region of interest (ROI) that limits the search for the needle to a small section of the image. The ROI consists of a square with a width of 10 times the needle radius. In frame j, the ROI is centred around the position of the needle found in frame $j-1$. Therefore, as the position of the needle moves in successive ultrasound images, the ROI moves accordingly such that the needle will always be located in the ROI. The Matlab function *imadjust* applies an intensity transformation to the image to improve the visibility of bright points. Next, we use an intensity threshold to obtain an average of candidate pixels for the needle shaft location within the axial image as shown in Fig. 8(b).

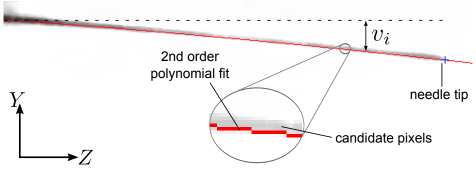

(a) Longitudinal image from the camera

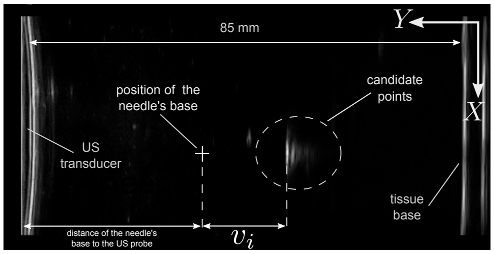

(b) Axial image from the ultrasound transducer

Fig. 8. Example of camera (a) and ultrasound images (b). In camera images, the obtained points after image processing are fit to a polynomial. In ultrasound images, the needle deflection is the distance along Y from the closest candidate point to the needle's base. In (b) the image is rotated by 90° with respect to Fig. 7.

B. Tissue Samples

The needle insertion experiments are performed using four different tissue samples shown in Fig. 9. First, for validation and assessment of the method, we use two different semitransparent phantom tissues with different mechanical properties. Homogeneous tissues and access to measurements of deflection with low noise provide an ideal scenario for validation of the proposed method. To demonstrate the feasibility of the proposed method using US images and non homogeneous tissue, we also use two different biological tissues.

Tissue 1 (see Fig. 9(a)) is made of industrial gelatin of porcine skin derived from acid-cured tissue (gel strength 300 from Sigma-Aldrich Corporation, Saint Louis, USA). A gelatin-based tissue is typically used due to its stable mechanical properties and similarity to human tissue characteristics. The concentration of the mixture is 127 grams of gelatin per litter of water that resulted in a Young's modulus of 55 kPa, measuring using indentation tests.

Tissue 2 (see Fig. 9(b)) is prepared with plastisol gel (M-F Manufacturing Co., Fort Worth, TX, USA). We use this plastisol tissue to test the proposed method in a tissue with high friction coefficient, as insertion velocity is not accounted for in our model. The viscous friction coefficient in Tissue 2

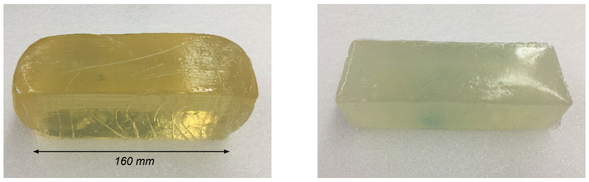

(a) Tissue 1 - Industrial gelatin (b) Tissue 2 - Plastisol gel

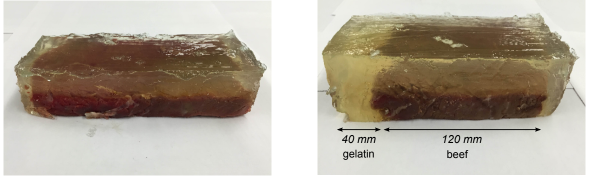

(c) Tissue 3 - Biological tissue (d) Tissue 4 - Gelatin-bio.

Fig. 9. Tissue samples used to validate the proposed method: (a) industrial gelatin, (b) high friction plastisol gel, (c) beef tenderloin, and (c) a two-layer tissue made of gelatin and beef.

is four times higher than in Tissue 1. We use a concentration ratio of 80% of liquid plastic and 20% of softener that yields a Young's modulus of 25.5 kPa, which is similar to the elastic modulus of human glandular tissue [15].

Tissue 3 (see Fig. 9(c)) is prepared by embedding a piece of beef tenderloin in the same gelatin preparation used for making Tissue 1. This biological tissue presents several layers of fat and some muscles, making it highly non homogeneous. The gelatin is meant to create a flat surface to ensure good acoustic contact between the US probe and the tissue. The needle is only inserted in the beef and never goes through the gelatin.

Tissue 4 (see Fig. 9(d)) is made of two different layers. The first layer is 40 mm wide and is made of the same gelatin used in Tissue 1. The second layer (roughly 120 mm wide) is a piece of beef tenderloin. The needle enters the tissue from the gelatin side and moves towards the biological tissue. To test the robustness of the proposed method, we will introduce an error in the model by assuming that Tissue 4 is homogeneous).

C. Transverse Tip Load Identification

One can estimate the forces applied at the needle tip during insertion (i.e., F, Q, and P) by measuring the necessary force for the needle to slice through the tissue [23]. This experiment is depicted schematically in Fig. 10. In order to minimize the needle bending during insertion, the needles are shortened for this particular experiment to a 90 mm length.

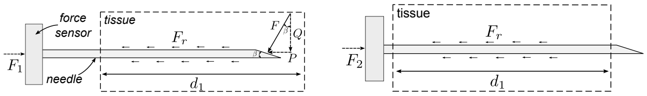

(a) Friction plus axial tip force (b) Friction force

Fig. 10. Identification of the transverse load. A short needle is inserted in a thin tissue and the horizontal insertion force is measured. In (a) the measured force F_1 is the axial component P of the cutting force F plus friction. In (b), the force F_2 corresponds to frictional effects only.

TABLE I
MEASURED FORCE APPLIED TO THE NEEDLE TIP DURING INSERTION.

Parameter		Tissue 1 (gelatin)	Tissue 2 (plastisol)	Tissue 3 (biological)	Tissue 4 (2 layers)
Axial force	P [N]	1.141	0.413	0.536	0.513
Transverse load	Q [N]	3.136	1.369	1.473	1.409
Q Standard dev.	σ [N]	± 0.234	±0.079	± 0.248	± 0.318

The needle is inserted throughout a thin tissue sample of thickness d_1 as shown in Fig. 10(a). During this phase, the measured axial insertion force at the needle's base increases with the insertion depth d since the measured force F_1 corresponds to the axial component P of the cutting force F plus the frictional force F_r generated along the shaft. Inertial effects are neglected since the needle is driven at a constant velocity. The insertion is carried on until the needle tip sticks out of the tissue. As soon as $d > d_1$, the force applied at the tip becomes zero (see Fig. 10(b)). Therefore, the measured force F_2 corresponds to friction only. The friction force per unit length is then obtained as $b = F_2 d_1^{-1}$. The axial component P of the cutting force F can be isolated by subtracting the measured friction from the total force F_1 as follows:

$$P = F_1(d) - \frac{F_2}{d_1} d \tag{15}$$

The transverse load Q is then calculated as $Q = P[\tan(\beta)]^{-1}$ where $\beta = 20^\circ$ is the tip bevel angle. The forces acting at the tip are assumed constant and, therefore, are unrelated to the insertion depth and the needle bending. Four different trials are performed for each tissue at 3 different constant insertion velocities, namely 5, 15, and 30 mm s^{-1}. The average value of the estimated tip forces and the standard deviation σ for the transverse load are summarized in Table I.

In this paper, we used insertion experiments to measure tip forces. In an *in vivo* interventional procedure, the tissue Young's modulus can be estimated using an US-based Acoustic Radiation Force Impulse (ARFI) imaging that relates the shear wave propagation speed of the US signal and the mechanical properties of the tissue [20]. Finally, the tissue stiffness can be related to the tip forces (i.e., F, P and Q) as proposed in [19]. Alternatively, tip forces can be estimated if images of the inserted needle are available for several different insertion depths. As we will see in the experimental results, the tissue parameter k_1 is constant for a given tissue. It is then possible to turn the optimization problem as a function of Q and k_0, and find the parameters that gives the same the simulated and measured deflections at several different insertion depths. The obtained Q can be used to estimate the needle deflection for other insertions with a single image.

VI. VERIFICATION IN PHANTOM AND EX-VIVO BIOLOGICAL TISSUE

In these experiments the needle is inserted five times to a depth of 140 mm into a tissue sample at two different constant insertion velocities of 5 and 30 mm s^{-1}. The US probe moves along with the needle such that the needle tip is always visible in the US image. Note that the US probe moves with the needle tip only for validation purposes. In fact, only a single image from this data is required. We will select a random insertion depth and tip position pair, called sampled data point, to serve as input to calibrate the proposed model. The algorithm is then used to estimate the past deflection and to predict future deflections for the insertion process.

Fig. 11 shows the predicted and measured needle tip deflection for the different tissues. For this set of experiments, the depth of the sampled data point is randomly fixed at 80 mm. The first plot of each image shows the results for a single insertion in each tissue. The second row shows the identified needle-tissue stiffness $K+T$. The error in predicting the tip position is shown in the third row. The fourth and fifth rows of plots show the average error obtained from all of the ten insertions in each tissue and its standard deviation, respectively.

Now, we will evaluate the performance of the model as the depth of the sampled data point varies from 0 mm (at the needle base) to 140 mm (maximum insertion depth). Fig. 12 shows the results as a function of the depth of the sampled data point. The proposed method does not work satisfactorily when the depth of the sampled data point is less then 30 mm, and therefore only the results for the sampled data points with depths between 30-140 mm are shown. The first row is the maximum error observed along the entire insertion depth. For a given sampled data point, we compute the maximum error as given in the third row of Fig 11. Then, we compute the average maximum error for this particular sampled data point over the ten insertions which is given by $\varepsilon_v = \frac{1}{10}\sum_{t=1}^{10} \max|\hat{v}_{n_j} - v_{n_j}|_t$. The second row of Fig. 12 shows the standard deviation of the maximum error. The third and fourth rows are the average error given by $\varepsilon_d = \frac{1}{10}\sum_{t=1}^{10}\left(\frac{1}{n-i_{end}}\sum_{j=n-i_{end}}^{m}|\hat{v}_{n_j} - v_{n_j}|\right)_t$ and its standard deviation. The error at the maximum insertion depth is shown in the fifth row.

As shown in Fig. 12, the proposed method works well when the depth of the sampled data point is more than 30 mm regardless of the tissue sample. An acceptable error in predicting needle deflection is 2 mm, as it corresponds to the diameter of the smallest detectable tumour in US images [1]. For the synthetic tissue samples, the average mean error and average maximum error remains bellow 2 mm as long as the depth of the sampled data point is more than 40 mm. For the biological tissue (Tissue 3) the minimum depth increases to 45 mm and for Tissue 4 (composed of two layers), it corresponds to 50 mm. For comparison purposes, the identified models parameters and the estimation error for all tissue samples for a depth higher than 50 mm are summarized in Table II.

A. *Discussion*

We tested the proposed model in four different tissue samples at two different needle insertion velocities.

Tissue 1 is the stiffest tissue sample. It resulted in the lowest standard deviation in identifying k_0 and k_1. The model prediction error is less than 2 mm as long as the depth of the sampled data point is larger than 40 mm. Given the low standard deviation, the results suggest that a single insertion attempt can be used to identify the model parameters to predict deflection in different insertion attempts.

In Tissue 2, the friction coefficient is four times higher than in Tissue 1. One can conclude that the performance of the model does not depend on the insertion velocity. Forces applied to the needle by the tissue as a result of increased needle insertion velocity will be accounted for in the calculated model parameter k_0. As for Tissue 1, the error remains bellow 2 mm for sampled data points acquired at an insertion depth higher than 40 mm.

Tissue 3 is *ex-vivo* biological and showed the highest radius of curvature among the samples. This is reflected in the obtained parameter value k_1 that is twice as high as for Tissue 1. For the error in estimating needle tip deflection to be less than 2 mm, the sampled data point must be acquired at a depth higher than 45 mm. This represents 32% of the maximum insertion depth.

Tissue 4 is composed of two distinct layers. The first one (40 mm width) is the same gelatin as in Tissue 1, and the second one (120 mm width) is a biological tissue similar to Tissue 4. Exepriment in this tissue presented the lowest model accuracy, since we considered in the model that the needle is inserted in a homogeneous tissue. The cutting force in the first 40 mm is almost three times higher than that in the subsequent 120 mm, resulting in a radius of curvature in the first layer higher than that in the second layer. Despite these differences, the model works satisfactorily as long as the insertion depth of the sampled data point is greater than 50 mm.

Two reasons contributed to the lower accuracy in the biological tissue when compared to the synthetic tissue: 1) We used cameras to measure the deflection in synthetic tissues and US images in biological tissues. US images often contain more noise compared to cameras images. Small uncertainties in localizing the needle shaft will result in high estimation errors. This explains why the minimum sampled data point must be acquired at a higher depth in the biological tissues compared to the synthetic tissues. 2) The proposed model assumes that the tissue is homogeneous and does not account for different layers as observed in biological tissues. It might result in deviations of the needle tip path from the previous radius of curvature followed by the tip.

The error in predicting the deflection is less than 2 mm and 1 mm when the input image is acquired at 35% and 50% or higher of the maximum insertion depth, respectively. This means that the US probe can be maintained at the same position throughout the insertion process.

VII. VERIFICATION IN IN-VIVO BIOLOGICAL TISSUE

In current prostate brachytherapy the probe is mounted on a stepper-stabilizer allowing the surgeon to take US images of the prostate at precise insertion depths. Although axial ultrasound images can be acquired at several depths, the surgeon does not have any means to predict the deeper deflection of the needle as it is further inserted in tissue. In this section, the utility of the proposed method for prostate brachytherapy applications is considered. We show that in-vivo needle deflection measurements obtained from ultrasound images during early stages of insertion can be used to predict the needle deflection further along the insertion process.

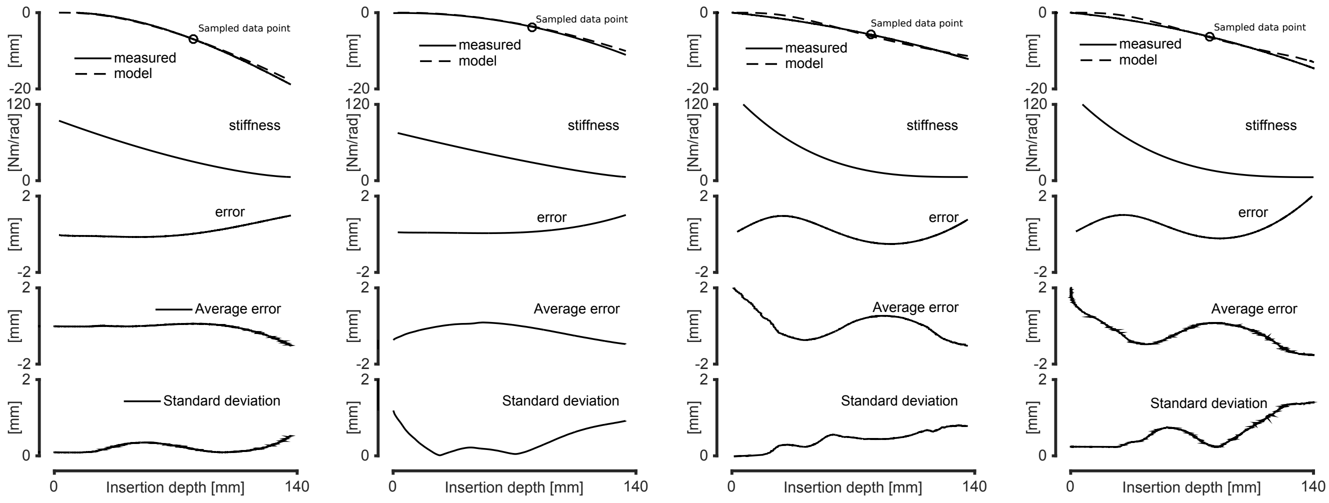

(a) Gelatin (b) Plastisol (c) Biological (d) Gelatin-biological

Fig. 11. Experimental results for each tissue sample. The needle tip deflection measured at 80 mm insertion depth is used as an input in the proposed method (sampled data point in the first row). The needle tip deflection is then predicted for all insertion depths. The first row shows the measured and predicted tip deflection for each tissue. The second and third row correspond respectively to the identified stiffness of the needle-tissue model and to the error in predicting needle tip deflection. The first there rows represent a single insertion. The average and the standard deviation of the error for all ten insertions performed into each tissue is shown in the fourth and fifth rows of graphs, respectively.

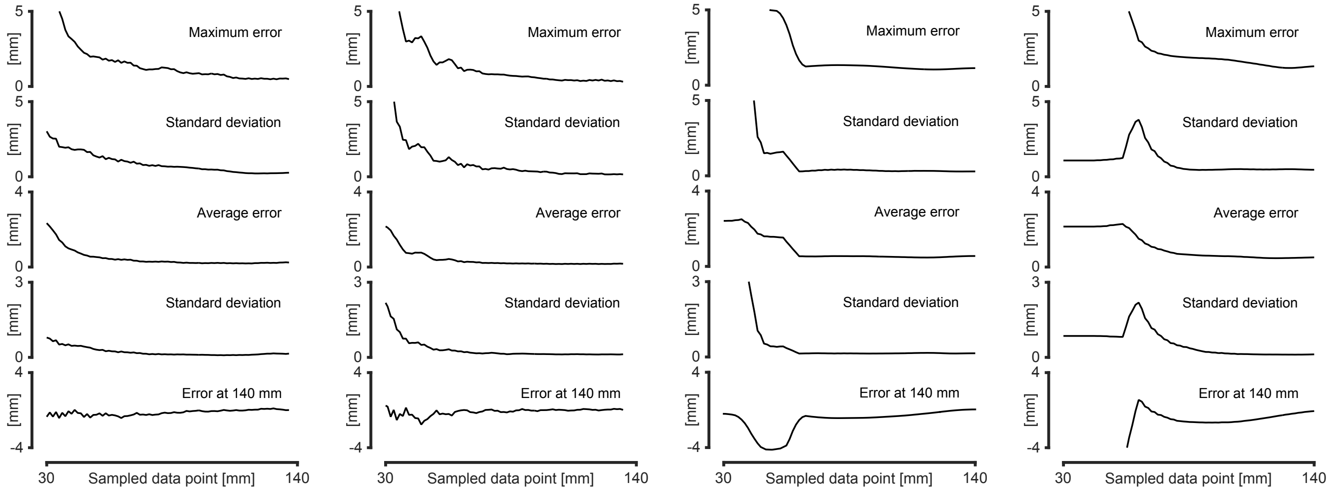

(a) Gelatin (b) Plastisol (c) Biological (d) Gelatin-biological

Fig. 12. Error in predicting needle deflection as a function of the depth of the sampled data point used for model parameters identification. The first and second rows show the average of the maximum error over ten insertion in each tissue sample and the standard deviation, respectivelly. The third and fouth rows present the average mean error and standard deviation, and the fihth row shows the error observed at the maximum insertion depth i.e. 140 mm.

TABLE II

IDENTIFIED MODEL PARAMETERS, AVARAGE AND MAXIMUM ERROR FOR NEEDLE DEFLECTION ESTIMATION

	Tissue samples							
	Gelatin		Plastisol		Biological		Gelatin-biological	
	Average	Deviation	Average	Deviation	Average	Deviation	Average	Deviation
k_0	0.2181	0.0070	0.3558	0.0327	0.8434	0.2927	0.8272	0.1183
k_1	1.5	0	1.2654	0.0446	3.1723	0.4635	3.0259	0.1970
Max error (mm)	1.0463	0.5119	0.8363	0.6228	1.2580	0.4950	1.8919	0.7461
Mean error (mm)	0.2895	0.1143	0.2380	0.1236	0.5363	0.1343	0.7246	0.3709
Error at 140 mm	0.3566	0.3295	0.3079	0.3281	0.6411	0.6389	0.9977	0.8101

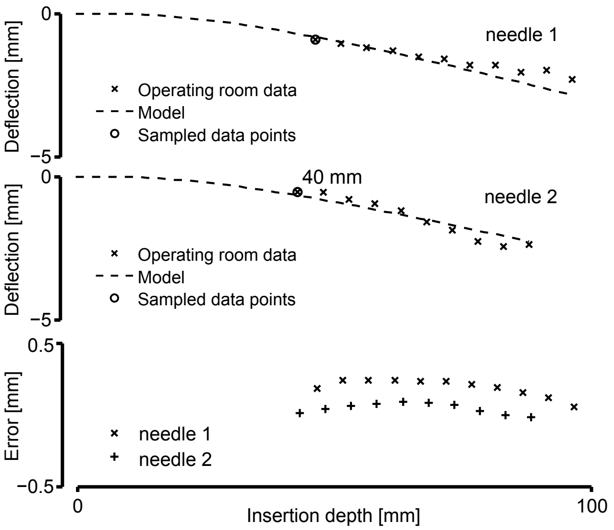

Fig. 13. Prediction of needle deflection during prostate brachytherapy. The deflection is obtained at an insertion depth of 40 mm from ultrasound images. The insertion depth is measured with respect to the patient's skin and images are only aquired after 40 mm.

Ultrasound images for prostate cancer patients undergoing permanent prostate brachytherapy were recorded during the procedure in the operating room. Axial images of the prostate with 5 mm incremental depths were acquired for two 18-gauges needles inserted at different depths. The insertion depth is measured with respect to the patient's skin. Image processing is used to determine the tip deflection at each insertion depth. We use the proposed method to estimate the needle deflection assuming that the deflection can only be measured at early stages of the insertion (i.e., the first visible point within the prostate at 40 mm depth). We assume that the normal load Q applied at the needle during *in-vivo* needle insertion is the same as the force measured in biological tissue in the previous section. We also assume that the location of the needle (i.e. in this example at 40 mm) has not changed from the time of needle insertion to the time of capture.

Fig. 13 shows the measured and predicted deflection for the first and second needles. Note that before 40 mm the needle is in contact with non-prostate tissue (transperineal fat). Usually, the complete brachytherapy procedure involves the insertion of about 20 needles. Hence, this model can be utilized to predict the needle deflection of subsequent needles, using the first or second needles to collect data for this model. The estimated error in predicting the needle deflection remains below 0.3 mm.

VIII. CONCLUSION

In this paper we proposed a new method to estimate the planar deflection of a needle based on the observation of deflection in a single transverse US image. To do so, we combined partial image observation with a needle-tissue interaction model. The needle model is composed of several rigid virtual links connected by virtual springs. We have shown that the stiffness of these virtual joints can be calculated using the mechanical properties of the needle. When the needle is inserted in the tissue, the reaction of the tissue is modelled as a modification of the stiffness of the virtual joints for those joints that are inside the tissue.

The proposed method was validated in two synthetic tissues and two *ex-vivo* biological tissues. The proposed model can predict the needle deflection with an error of less than 2 mm as long as the image used in the model is acquired at a depth that corresponds to 35% or more of the maximum insertion depth. This is done by combining a single US image and the needle-tissue model. To solve the model adaptively as the needle is inserted, we proposed an optimization method based on a pattern search algorithm that calculates the model parameters and allows us to predict the needle deflection further along the insertion process. The US probe can be maintained at the same position during the insertion of the needle; therefore, complications of tissue deformation caused by the motion of the US probe are avoided.

Application of the proposed method to *in-vivo* brachytherapy showed that needle deflection can be estimated with an average error of less than 0.3 mm. The deflection measured at the early stages of insertion can be use to collect data and predict the deflection across different insertion attempts.

The current processing time of 0.7 sec allows the method to be integrated in US images to display the path followed by the needle tip and future deflection of the needle in real time, which provides valuable information to surgeons performing US image-guided needle insertion.

COMPLIANCE WITH ETHICAL STANDARDS

All procedures performed in studies involving human participants were in accordance with the ethical standards of the institutional and/or national research committee and with the 1964 Helsinki declaration and its later amendments or comparable ethical standards. Informed consent was obtained from all individual participants included in the study. Approval for the study granted by the Alberta Cancer Research Ethics Committee under file number 25837.

CONFLICT OF INTERESTS

The authors declare that they have no conflict of interest.

REFERENCES

[1] Abayazid, M., Roesthuis, R., Reilink, R., Misra, S.: Integrating deflection models and image feedback for real-time flexible needle steering. Robotics, IEEE Transactions on **29**(2), 542–553 (2013)

[2] Abolhassani, N., Patel, R., Ayazi, F.: Needle control along desired tracks in robotic prostate brachytherapy. In: Systems, Man and Cybernetics, 2007. ISIC. IEEE International Conference on, pp. 3361–3366. IEEE (2007)

[3] Beer, F.P., Sanghi, S.: Mechanics of materials, 6th ed., global ed. / adapted by sanjeev sanghi edn. New York, N.Y. : McGraw-Hill (2012). Includes index

[4] Bogdanich, W.: At VA hospital, a rogue cancer unit. The New York Times. June **20** (2009)

[5] Chapman, G.A., Johnson, D., Bodenham, A.R.: Visualisation of needle position using ultrasonography. Anaesthesia **61**(2), 148–158 (2006). DOI 10.1111/j.1365-2044.2005.04475.x

[6] Chin, K.J., Perlas, A., Chan, V.W., Brull, R.: Needle visualization in ultrasound-guided regional anesthesia: Challenges and solutions. Regional Anesthesia and Pain Medicine **33**(6), 532 – 544 (2008)

[7] Dehghan, E., Goksel, O., Salcudean, S.E.: A comparison of needle bending models. In: Medical Image Computing and Computer-Assisted Intervention–MICCAI 2006, pp. 305–312. Springer (2006)

[8] Fischler, M.A., Bolles, R.C.: Random sample consensus: a paradigm for model fitting with applications to image analysis and automated cartography. Communications of the ACM **24**(6), 381–395 (1981)

[9] Glozman, D., Shoham, M.: Image-guided robotic flexible needle steering. Robotics, IEEE Transactions on **23**(3), 459–467 (2007). DOI 10.1109/TRO.2007.898972

[10] Goksel, O., Dehghan, E., Salcudean, S.E.: Modeling and simulation of flexible needles. Medical Engineering & Physics **31**(9), 1069 – 1078 (2009)

[11] Gonzales, R.C., Woods, R.E.: Digital Image Processing, 2-nd Edition. Prentice Hall (2002)

[12] Haddadi, A., Hashtrudi-Zaad, K.: Development of a dynamic model for bevel-tip flexible needle insertion into soft tissues. In: Engineering in Medicine and Biology Society, EMBC, 2011 Annual International Conference of the IEEE, pp. 7478–7482. IEEE (2011)

[13] Hong, J., Dohi, T., Hashizume, M., Konishi, K., Hata, N.: An ultrasound-driven needle-insertion robot for percutaneous cholecystostomy. Physics in Medicine and Biology **49**(3), 441 (2004)

[14] Khadem, M., Fallahi, B., Rossa, C., Sloboda, R., Usmani, N., Tavakoli, M.: A mechanics-based model for simulation and control of flexible needle insertion in soft tissue. In: Robotics and Automation (ICRA), 2015 IEEE International Conference on, pp. 2264–2269 (2015)

[15] Krouskop, T.A., Wheeler, T.M., Kallel, F., Garra, B.S., Hall, T.: Elastic moduli of breast and prostate tissues under compression. Ultrasonic Imaging **20**(4), 260–274 (1998)

[16] Lachaine, M., Falco, T.: Intrafractional prostate motion management with the clarity autoscan system. Med. Phys. Int **1**(1), 72–80 (2013)

[17] Lehmann, T., Rossa, C., Usmani, N., Sloboda, R., Tavakoli, M.: A virtual sensor for needle deflection estimation during soft-tissue needle insertion. In: Robotics and Automation (ICRA), 2015 IEEE International Conference on, pp. 1217–1222 (2015)

[18] Mathiassen, K., Dall'Alba, D., Muradore, R., Fiorini, P., Elle, O.J.: Real-time biopsy needle tip estimation in 2d ultrasound images. In: Robotics and Automation (ICRA), 2013 IEEE International Conference on, pp. 4363–4369. IEEE (2013)

[19] Misra, S., Reed, K., Schafer, B., Ramesh, K., Okamura, A.: Mechanics of flexible needles robotically steered through soft tissue. The International Journal of Robotics Research **29**(13), 1640–1660 (2010). DOI 10.1177/0278364910369714

[20] Moreira, P., Misra, S.: Biomechanics-based curvature estimation for ultrasound-guided flexible needle steering in biological tissues. Annals of Biomedical Engineering pp. 1–11 (2014). DOI 10.1007/s10439-014-1203-5

[21] Nag, S., Bice, W., DeWyngaert, K., Prestidge, B., Stock, R., Yu, Y.: The american brachytherapy society recommendations for permanent prostate brachytherapy postimplant dosimetric analysis. International Journal of Radiation Oncology* Biology* Physics **46**(1), 221–230 (2000)

[22] Neubach, Z., Shoham, M.: Ultrasound-guided robot for flexible needle steering. Biomedical Engineering, IEEE Transactions on **57**(4), 799–805 (2010)

[23] Okamura, A., Simone, C., O'Leary, M.: Force modeling for needle insertion into soft tissue. IEEE Transactions on Biomedical Engineering **51**(10), 1707–1716 (2004). DOI 10.1109/TBME.2004.831542

[24] Okazawa, S.H., Ebrahimi, R., Chuang, J., Rohling, R.N., Salcudean, S.E.: Methods for segmenting curved needles in ultrasound images. Medical image analysis **10**(3), 330–342 (2006)

[25] Schlosser, J., Salisbury, K., Hristov, D.: We-d-220-01: Tissue displacement monitoring for prostate and liver igrt using a robotically-controlled ultrasound system. Medical Physics **38**(6), 3812–3812 (2011)

[26] Spong, M.W., Vidyasagar, M.: Robot dynamics and control. John Wiley & Sons (2008)

[27] Vrooijink, G.J., Abayazid, M., Patil, S., Alterovitz, R., Misra, S.: Needle path planning and steering in a three-dimensional non-static environment using two-dimensional ultrasound images. The International Journal of Robotics Research p. 0278364914526627 (2014)

[28] Waine, M., Rossa, C., Sloboda, R., Usmani, N., Tavakoli, M.: 3D shape visualization of curved needles in tissue from 2D ultrasound images using ransac. In: Robotics and Automation, 2015 IEEE International Conference on, pp. 4723–4728. IEEE (2015)

[29] Yan, P., Cheeseborough, J.C., Chao, K.C.: Automatic shape-based level set segmentation for needle tracking in 3-d trus-guided prostate brachytherapy. Ultrasound in medicine & biology **38**(9), 1626–1636 (2012)